Saharan aerosol sensed over Warsaw by backscatter depolarization lidar

Aleksandra E. KARDAS[1], Krzysztof M. MARKOWICZ[1], Kamil STELMASZCZYK[2], Grzegorz KARASIŃSKI[3], Szymon P. MALINOWSKI[1], Tadeusz STACEWICZ[3], Ludger WOESTE[2], Carsten HOCHHERTZ[2]

[1]Institute of Geophysics, University of Warsaw, Pasteura 7, 02-093 Warsaw, Poland

[2]Free University of Berlin, Physics Department, Arnimallee 14, D-14195 Berlin, Germany

[3]Institute of Experimental Physics, University of Warsaw, Hoża 69, 00-681 Warsaw, Poland

*Corresponding author: tadeusz.stacewicz@fuw.edu.pl

The estimates of the optical properties of mineral dust aerosol observed on April 13th and 14th, 2005 during SAWA (Saharan aerosol over Warsaw) experiment are described.

Lidar signals at 532 and 1064 nm wavelengths were inverted with a modified Klett–Fernald algorithm. Aerosol optical depth measured with a sun-photometer allowed to reduce uncertainties in the inversion procedure. Further improvement of the estimation came from distinguishing three aerosol layers in the atmosphere on the basis of vertical profiles of optical properties.

Having calculated vertical distributions of aerosol extinction coefficients, profiles of local Angstrom exponent were estimated. Independent information on depolarisation of 532 nm lidar returns, together with the assumption about the spheroidal shape and random orientation of aerosol particles, allowed to estimate the aspect ratio and size of particles on the basis of numerical calculations with transition matrix (T-matrix) algorithm by M. Mishchenko. Results indicate the mode radii of spheroids in the range of $0.15-0.3$ μm, and their aspect ratio in the range of $0.6-0.8$ or $1.3-2.2$ (two solutions are allowed). Small size of the particles is explained by dust deposition and mixing with boundary layer aerosol in the Mediterranean region.

Keywords: aerosol, mineral dust, long-range aerosol transport, remote sensing.

1. Introduction

It is commonly known that aerosol effect on climate is important and complex [1]. For many aerosol types it is not yet established, whether their net contribution to the Earth surface heat balance is positive or negative [2]. Among these types there is mineral dust [1] emitted from the Earth surface in desert areas and transported in the atmosphere at long distances [3, 4]. Typical source areas of dust events observed in Europe are Sahara and Arabian deserts [4, 5].

In this paper we describe the investigation of the optical properties of mineral dust transported in the middle troposphere from Sahara and Arabian deserts over Poland. The measurements were performed during a particular dust episode of 13–14 April 2005. Dust plume, originating in Arabian Desert and Sahara, carried by flow from south, drifted over Europe reaching Warsaw (52N, 21E) [6]. Such events are common in Europe, most often during the spring time [5, 7–10]. There are several reports on the optical properties of desert aerosols observed, *e.g.*, in Germany [9, 11] or Scandinavia [12]. However, the number of reports from Central and Northern Europe, *e.g.* [13], is small compared to that from the southern part of the continent, *e.g.*, [5, 8, 13–21]. Therefore, the properties of desert aerosol transported towards north remain an interesting issue. This was a motivation for a research campaign Saharan aerosol over Warsaw (hereafter referenced as SAWA), which was conducted in spring 2005 in the emerging aerosol/radiative transfer laboratory of the University of Warsaw [6].

The key instruments used were sun-photometers: Microtops and a prototype multi-spectral device [22] as well as the aerosol lidar (Teramobile Profiler from the Free University of Berlin) described more closely in Section 2. Data collected with these instruments were analyzed, taking a special concern in synergy of the measurements.

One of the goals of the SAWA campaign was finding a simplified representation of the dust particles, suitable for a radiative transfer model. The main idea was to use information on the aerosol optical depth obtained from passive photometers in order to reduce the number of assumptions necessary to invert the lidar signal in spirit of [23, 24]. Then, with an additional postulate that the dust particles may be represented by an ensemble of randomly oriented spheroids [25], the size and aspect ratio of the observed dust particles were estimated. Transition matrix (T-matrix) algorithm [25] was used in order to calculate scattering properties of the non-spherical aerosol. Applicability of such models has already been studied by, *e.g.*, [26, 27].

2. SAWA measurement campaign

2.1. Mineral dust event

SAWA campaign took place in April and May 2005, in Warsaw. In order to plan the intensive measurement periods, a long range Navy Aerosol Analysis and Prediction System (NAAPS), available at Naval Research Laboratory Monterey Aerosol Page (http://www.nrlmry.navy.mil/aerosol/), was used as a forecast tool. The situation was in parallel monitored, using satellite imagery (MODIS, AVHRR).

One major dust event (12–19 April) occurred within the time frame of the experiment. The most complete data, comprising synergistic lidar and sun--photometer measurements, were collected on April 13th and 14th.

In order to illustrate the development of the dust event during the measurement period, the range corrected, vertically smoothed lidar returns in 532 nm wavelength

are presented in Fig. 1**a**. Figure 1**b** shows a profile from 23:58 UTC, 13 April 2005, with layers identification marked. This signal reflects the nocturnal atmospheric boundary layer (ABL) structure: a stable layer below 540 m and a residual layer between 540 m and 1.2 km. Two distinct regions of increased lidar returns can be noticed in Fig. 1. The first one, spanning from the surface to 1.5 km denoted as BL, encloses the ABL. The second one, denoted as DD (desert dust), is located above ABL
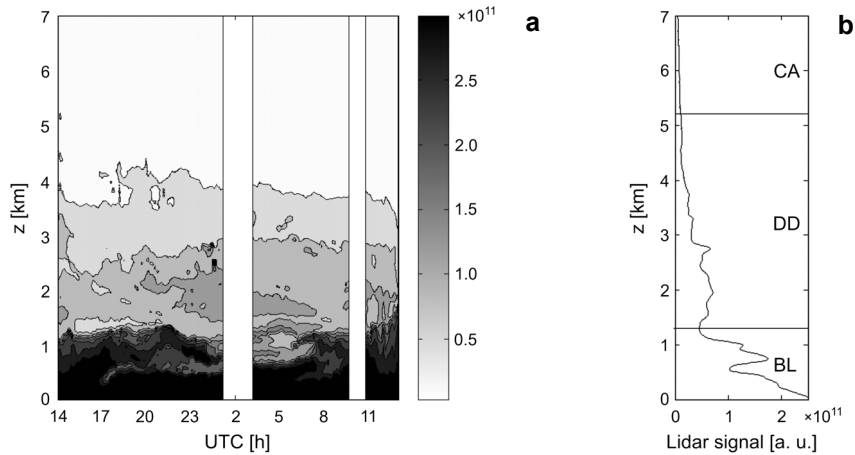

Fig. 1. Temporal evolution of lidar returns (**a**) recorded for 532 nm wavelength on 13–14 April 2005 in Warsaw (arbitrary units). Light and moderate grey areas located between 1.2 and 4 km correspond to the mineral dust layer. Above, very weak signals of the free troposphere may be seen. Exemplary lidar profile (**b**), 23:58 UTC, 13 April 2005 with marked layers identification: BL – boundary layer aerosol, DD – desert dust aerosol, CA – "clear air". This signal reflects the nocturnal boundary layer structure – stable layer below 540 m and residual layer between 540 m and 1.2 km. Layer structure – stable layer below 540 m and residual layer between 540 m and 1.2 km.
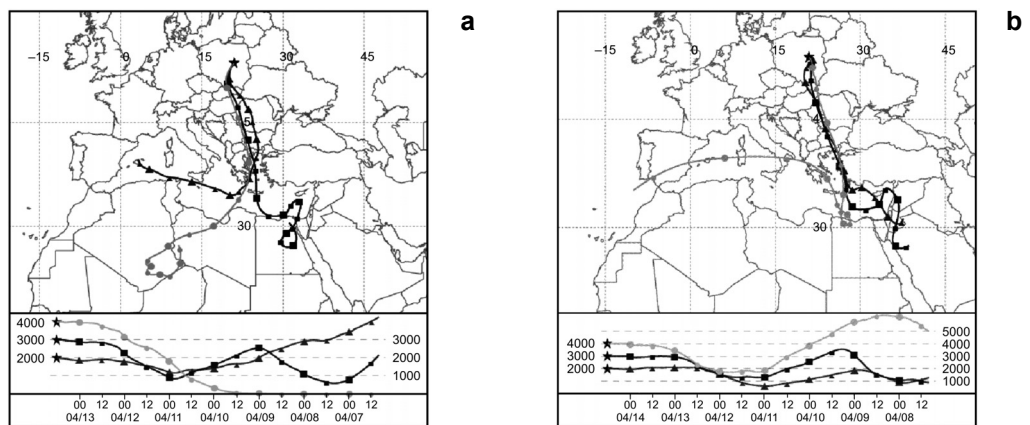

Fig. 2. Backward trajectories for 13 (**a**) and 14 (**b**) April 2005 calculated with the HYSPLIT model. Both for 172 hours backward. The panels below maps show the horizontal projection of the trajectories with their positions marked every 12 hours.

and spans up to 4−5 km height. It results from back-scatter due to enhanced aerosol concentration in the free troposphere and in Fig. 1**a** it is visualized in shades of gray. DD layer is topped by clear atmosphere, denoted as CA. More on the distinguishing between the layers can be found in Section 4.1.

Presence of a DD over BL is in agreement with the prediction of NAAPS model, which showed a dust plume transported in the middle troposphere from the regions of Sahara and Middle East. To closer affirm NAAPS results and lidar return observations, backward trajectories were calculated with hybrid single-particle Lagrangian integrated trajectory (HYSPLIT) model [28, 29]. Figure 2**a** shows that the source region of air masses observed on 13 April in Warsaw at the heights of 3−4 km is Sahara. Figure 2**b** (14 April) points also at the northern regions of Arabian Peninsula.

2.2. Instrumentation and data quality

The photometric data discussed here were collected with the use of a hand-held Microtops II (Solar Light Co.) sunphotometer, measuring direct solar radiation in five channels: 380, 440, 500, 675 and 870 nm, with resolution of 0.1 W/m^2. Its built-in algorithm produces total aerosol optical depth (AOD) in each channel. The instrument was recalibrated with Langley technique [30]. Estimated accuracy of measurements was better than 5%. Microtops results for April 13th and 14th were compared to the CIMEL records from the nearby (about 50 km south) AERONET station in Belsk [31]. Since the channels of both instruments do not exactly overlap, the CIMEL measurements at 673 nm were compared with Microtops measurements in 675 nm and AOD values for 673 nm interpolated from Microtops measurements with the use of Angstrom formula [32]. The average differences between results were less than 6.5% in both cases.

Lidar measurements were taken with Teramobile Profiler. It is a multi-wavelength back-scattering lidar, based on a solid state 10 Hz Nd:Yag laser (Big Sky Laser CFR 200), which delivers 10 ns long pulses of energies of 60, 50, 30 mJ, in 1064, 532 and 355 nm wavelengths, respectively. As a receiver, the lidar uses F4/200 mm Newtonian telescope. Unfortunately, as it was noticed later, the UV channel of the lidar was not operating correctly and its records were not accounted in the analysis. In aerosol measurements 7 km range was taken into consideration.

Optical system of the Teramobile Profiler has a multi-axial design, in which each wavelength is emitted as a separate beam. The inclination of each beam can be individually adjusted assuring fairly equal overlap with telescope's field-of-view, which compensates the geometrical compression effect, limiting it to the heights of 260−280 m. More details on the system can be found in [33].

To account for geometrical compression, the signal was divided by an overlap function, varying between 0 and 1 [23, 24]. Finding the overlap function requires recording lidar signal back-scattered in a homogeneous atmosphere. In such conditions, the range corrected lidar returns (X, see also Section 3.1) can be written as:

$$X(z) \;=\; O(z)C\beta \exp(-2az) \tag{1}$$

where z is the vertical coordinate, $O(z)$ defines the overlap function, C is the lidar constant, β and a are back-scatter and extinction coefficients. Outside the geometrical correction range $O(z) = 1$, so Eq. (1) can be rewritten as:

$$\ln[X(z)] \;=\; \ln(C\beta) - 2az \tag{2}$$

Parameters $C\beta$, $2az$ may be determined with the linear regression of Eq. (2) and substituted in Eq. (1) to derive the overlap function. Typically, in order to run this procedure, horizontal lidar shots are performed [23]. As the Teramobile Profiler can measure only vertical distributions [33], we had to derive overlap function from vertical profiles collected in a well-mixed atmospheric boundary layer. Noon of April 13th, 2005 was selected for this purpose, on a basis of aerological sounding from nearby (20 km NE from the measurement site) WMO 12374 station. The sounding shows an adiabatic, dry (relative humidity from 42% at the surface to 60% at the top), ABL of thickness of 1150 m from the ground, capped with the inversion of 1.2 °C. The accuracy of the overlap correction was estimated in these well-mixed conditions at 15% in the lowest 50 m layer, 10% at 150 m and less than 5% near the geometrical compression range.

The back-scattered light collected by the telescope was spectrally separated. Its intensity was measured independently at each wavelength with the photo-multipliers (Hammamatsu R7400 -P04 and -U02 for 355 and 532 nm) and with the avalanche photo-diode (EG&G C30954/5E for 1064 nm). All signals were recorded with a 12-bit, 20 MHz transient recorder (Licel) assuring vertical spatial resolution of 7.5 m. Data were then averaged over 1000 laser shots (~1 min).

Intensity of the 532 nm signal was measured by two photomultipliers in polarizations parallel and perpendicular to that of the emitted beam. In order to minimize the depolarization error caused by the receiver optics, all bending mirrors of the detection system were coated with the phase optimized dielectric coatings. In this way the elliptical polarization was avoided and the cross-talk between parallel and perpendicular polarization channels was effectively reduced. The only component with an ordinary (not phase optimized) high reflection coating was the telescope primary mirror. However, the nearly normal incidence of the incoming light, together with the large curvature radius of this mirror, leads to the depolarization of less than 0.01.

To compensate the electro-optical efficiencies for parallel and perpendicular detection channels, a calibration routine was performed before each measurement series (once in a couple of hours). First, the laser polarization was matched to the detection polarization axis and the lidar signal for the parallel polarization was measured. Then, the laser polarization was turned by 90°[*] and the same lidar signal was measured with the cross polarization detection channel. The gain of the photomultiplier used for the cross polarization was then set to match the signal

---

[*]During the calibration, the laser polarization was turned by the zero-order half-wavelength plate mounted at the laser beam output. A clean polarization of light after the half wavelength plate was accomplished by the Glan Laser prism located directly before the retardation plate.

intensity of the parallel polarization and remained unchanged during the following measurement series. Because the photomultipliers used for parallel and cross polarizations are almost identical (the same manufacturing series) the similar HV was applied in both cases. This allowed to assume the same gain factor for strong and weak signals. Finally, the laser was set up to the original polarization and the measurements were performed.

In real atmosphere retrieving depolarization due to aerosol particles requires accounting for depolarization by air molecules (Rayleigh scattering). We used the formula proposed by [34]:

$$\delta(z) = \frac{\delta_{tot}(B + B\delta_{ray} - \delta_{ray}) - \delta_{ray}}{B - 1 + B\delta_{ray} - \delta_{tot}} \tag{3}$$

where B is the total to Rayleigh back-scattering coefficient ratio, δ_{ray} – the molecular depolarization (assumed 0.00365 after [35]) and δ_{tot} – total depolarization:

$$\delta_{tot} = \frac{X_R}{X_L} \tag{4}$$

here X_R and X_L are the values of range corrected lidar returns with polarizations perpendicular and parallel to the polarization of the original beam [36], respectively.

3. Data processing

3.1. Lidar signal inversion method

The analysis of lidar returns is based on the classical Klett–Fernald algorithm introduced in [37, 38]. Lidar equation is solved in terms of range corrected signal X and transmittance (T_R – molecular, T_A – aerosol) with an assumption of linear relationship between extinction and backscattering coefficient. The following formula is used in the calculations:

$$\beta_A(z) = \frac{X(z)T_R^{2(r-1)}(z)}{C - 2S_A(z)\int X(z')T_R^{2(r-1)}(z')\mathrm{d}z'} - \beta_R(z) \tag{5}$$

where β_R and β_A are backscatter coefficients for molecules and aerosol particles, z is the distance from the lidar (height), C is the lidar constant, $S_A(z)$ is the aerosol extinction to back-scatter ratio (lidar ratio), and

$$r(z) = \frac{S_A(z)}{S_R} \tag{6}$$

($S_R = 8\pi/3$ is the backscatter to extinction ratio for Rayleigh scattering.)

Computations begin at the top of the measurement range, by assumption $\beta_A(z_{max}) = 0$. Then pairs of equations similar to Eq. (5), written for subsequent levels in the atmosphere, z and $z = dz$ are solved. This allows to avoid the necessity of establishing the value of the lidar constant C [23]. $\beta_R(z)$ is usually calculated with empirical equations for assumed or measured vertical profiles of temperature and pressure in the atmosphere [24].

At this point, a remaining unknown S_A is evaluated with the iterative procedure. In the first step, some typical value of S_A is assumed (this initial assumption does not influence the final result). Then, after calculating the whole vertical profile of β_A, S_A is redefined as:

$$S_A = \frac{\tau_{SP}}{\int \beta_A(z)dz} \qquad (7)$$

where τ_{SP} is the total optical depth of aerosol, measured with the sun-photometer [23]. The calculations begin again at the top of the range and the procedure is repeated until the difference between subsequent values of S_A is smaller than 0.0001.

When aerosol properties are dependent of height, the above procedure gives the average S_A [23]. During SAWA we observed three significantly different aerosol layers (for the details of division see Section 4) and focused on the properties of one of them (desert dust – DD). Therefore, we decided to modify the procedure by performing separate calculations for each layer.

In the first step, the extinction coefficient profiles were calculated for the whole atmosphere, taking into account the total AOD measured by the sun-photometer.
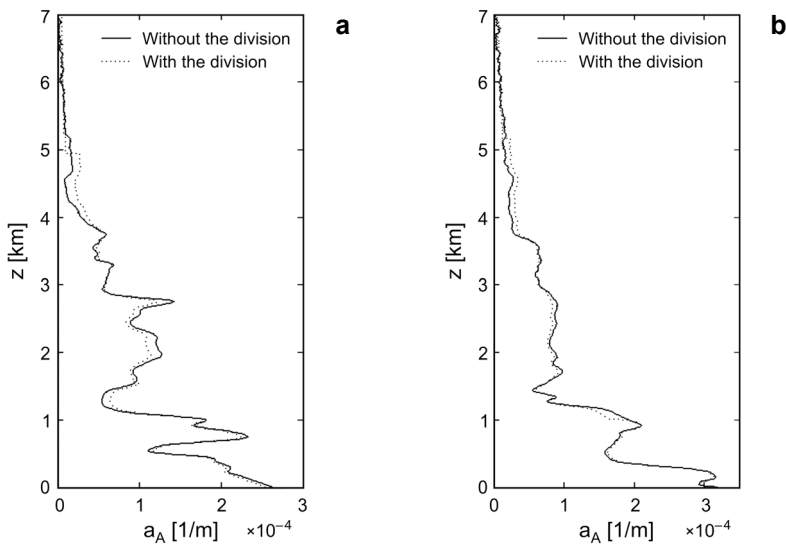

Fig. 3. Aerosol extinction coefficient a_A profiles calculated with and without the division of atmosphere into layers. 532 nm wavelengths, 23:58 UTC, 13 April (**a**), 09:30 UTC, 14 April 2005 (**b**).

Then, the integration of the extinction coefficient within specified height ranges (see Section 4) gave approximated optical depths of individual layers (to be used instead of τ_{SP} while running the algorithm for each layer separately).

Fully reliable error analysis of this procedure would require independent AOD measurements on different levels (in case of SAWA 13–14 April observations: 0 km, about 1.5 km, and about 5 km) which, unfortunately, was not possible. Figure 3 demonstrates differences between instantaneous extinction profiles estimated with and without division of the atmosphere into three layers. Differences are not big, but observable. For BL the modifications in the extinction coefficient profile are usually small, for DD layer maximum modification reaches up to 35% of the estimated value. Estimates with division seem smoother and less noisy than that with the single layer approach.

3.2. Numerical calculations (T-matrix)

One of the goals of the SAWA campaign was to find a mathematical representation of dust particles, suitable for a radiative transfer model. The transition matrix (T-matrix) method, initially developed by [39] and implemented by [25][*], was selected as a suitable tool. T-matrix is very useful in modeling the interaction between light and an ensemble of randomly oriented particles. Particles considered may be of arbitrary shapes, but the formulas simplify decidedly, when a rotational symmetry is assumed.

An assumption that the observed dust particles could be represented by an ensemble of randomly oriented spheroids [40] of single-mode log-normal size distribution and fixed aspect ratios was adopted[**]. Then the look-up tables allowing to determine optical properties of aerosols were created (Sections 3.3 and 3.4). They cover the following ranges of physical properties of aerosol particles: the aspect ratios between 0.25 (prolate spheroids) and 4.0 (oblate spheroids); the mode radii in the range of $0.01–1.0$ µm for fixed mode width of 0.5; the refractive index of $1.53 + 0.008i$ for 532 nm wavelength (selected after OPAC software package [41]).

Sensitivity tests consisting of changing the real part of the refractive index in the range of $1.5–1.6$ [42, 43] and changing the order of magnitude of its imaginary part were performed. Results of these tests were used in estimating the uncertainties of particle size and shape evaluation (Sections 3.3 and 3.4).

3.3. Estimation of particles' size

Estimates of the mean size of the particles were performed using the values of the Angstrom exponent. Angstrom empiric power law [32] describes the relationship between radiation extinction on aerosol particles and wavelength λ:

---

[*]FORTRAN routine available at http://www.giss.nasa.gov/~crmim/t_ matrix.html.
[**]Since the reliable lidar returns were recorded in 2 channels only, an assumption of bimodal distribution function could not be applied.

$$a_A = \xi\lambda^{-\alpha} \tag{8}$$

where ξ – Angstrom coefficient, α – Angstrom exponent. It is valid for most kinds of aerosol.

T-matrix simulations of the light transfer through an ensemble of particles (Section 3.2) for a number of different mode radii show that at least within a limited particle radius range (0.1–0.6 μm), the relationship between α and the mean radius is monotonic and shape-independent. This is presented in Fig. 4, where the plots corresponding to different spheroids aspect ratios overlap (three aspect ratio values were chosen as a representative for different particle types: 2 corresponding to oblate spheroids, 0.5 – prolate spheroids, 1 – spheres). Thus, Fig. 4 can be used to estimate the mode radius of spheroids, on the basis of α. Angstrom exponent was evaluated from the distributions of extinction coefficient at various lidar wavelengths.

Table 1 with the results of selected numerical tests illustrates the impact of assumed refractive index variation on the estimated mode radii. For instance, changing the real part of the refractive index by 0.03 results in ~6% variation of the mode radii for $\alpha \le 1$ and ~3% for $\alpha > 1$. In case of absorption change by a factor of 10, the mode radii varies
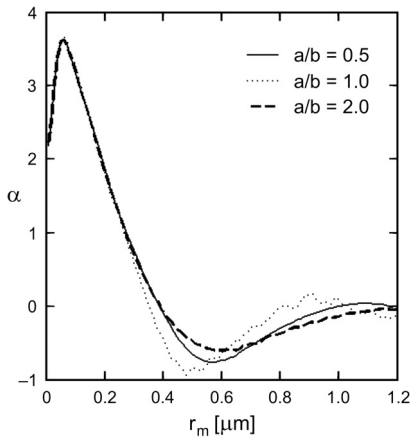

Fig. 4. Angstrom exponent α dependency of the mode radius r_m of randomly oriented spheroids with a log-normal size distribution, calculated for the refractive index of sand and various aspect ratios (a/b). In the radii range of 0.1–0.6 μm, the relationship between α and the mean radius is monotonic and shape-independent.

T a b l e 1. Exemplary results of T-matric calculation for different refractive indices – look-up table for particle mode radius r_m [μm] on the basis of Angstrom exponent α.

α	Refractive indices for 532 nm				
	$1.50 + 0.008i$	$1.53 + 0.008i$	$1.56 + 0.008i$	$1.60 + 0.008i$	$1.53 + 0.08i$
0.5	0.33	0.31	0.29	0.28	0.29
1.0	0.28	0.27	0.26	0.24	0.25
1.5	0.24	0.22	0.22	0.21	0.20
2.0	0.19	0.19	0.18	0.18	0.17
2.5	0.16	0.16	0.15	0.15	0.13

by ~20% for $\alpha > 2$, by ~10 % for $1 < \alpha < 2$, and by ~5% for $\alpha \leq 1$. There is no significant change for $r_m \approx 0.4$ μm.

3.4. Estimation of particles' shape

Results of T-matrix simulations for various mode radii of aerosol particles (Fig. 5) confirm that δ can be used in estimates of the particle ratio. Its value is zero for spheres and is decidedly higher for spheroids (single scattering). Unfortunately, the result is not unequivocal – there are at least two possible aspect ratios for a given mode radius and depolarization.

Numerical tests indicate that the bigger the depolarization and the smaller the mode radii, the more the procedure is sensitive to the choice of the assumed refractive index.
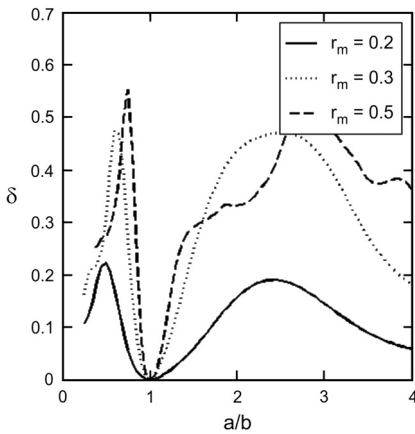

Fig. 5. Depolarization δ dependency of the aspect ratio (a/b) of randomly oriented spheroids with a log-normal size distribution, calculated for the refractive index of sand and different mode radii r_m [μm]. The value always reaches 0 for spherical particles ($a/b = 1$).

T a b l e 2. Exemplary results of T-matrix calculation for different refractive indices – look-up table for aspect ratio on the basis of depolarization δ and mode radius r_m [μm]. Pairs of values are presented – for prolate and oblate spheroids.

δ	r_m [μm]	Refractive indices for 532 nm									
		$1.50 + 0.008i$		$1.53 + 0.008i$		$1.56 + 0.008i$		$1.60 + 0.008i$		$1.53 + 0.08i$	
0.10	0.15	–	–	0.41	–	0.47	–	0.54	–	0.43	–
	0.20	0.66	1.88	0.69	1.71	0.71	1.60	0.74	1.50	0.72	1.72
	0.25	0.78	1.42	0.79	1.38	0.80	1.35	0.81	1.33	0.84	1.26
	0.30	0.83	1.28	0.84	1.27	0.84	1.27	0.84	1.28	0.87	1.19
0.13	0.15	–	–	–	–	–	–	0.45	–	–	–
	0.20	0.61	2.22	0.65	1.85	0.68	1.71	0.71	1.59	0.68	–
	0.25	0.75	1.50	0.77	1.45	0.78	1.41	0.78	1.39	0.81	1.33
	0.30	0.81	1.33	0.82	1.32	0.82	1.32	0.82	1.33	0.86	1.22
0.16	0.15	–	–	–	–	–	–	–	–	–	–
	0.20	0.57	–	0.61	2.02	0.64	1.82	0.68	1.68	0.64	–
	0.25	0.73	1.58	0.74	1.52	0.76	1.48	0.76	1.45	0.79	1.39
	0.30	0.80	1.38	0.80	1.37	0.80	1.37	0.80	1.38	0.84	1.26

Table 2 presents selected results of calculations for particles of mode radii between 0.15 and 0.3 μm. For mode radii <0.2 μm the representative aspect ratio often may not be retrieved. In such a case, variation of the refractive index within assumed values may cause even a 30% change of the estimated aspect ratio. Here we focus on prolate spheroids. Changing the imaginary part of refractive index by the factor of 10 modifies the estimated aspect ratios by ~5%. In case of mode radii ~0.2 μm, changing the real part of refractive index by 0.03 modifies the evaluation by 5–6%. For bigger particles, the modifications reach ~3% the most.

4. Results

4.1. AODs and extinction

During SAWA experiment, total aerosol optical depths were measured with Microtops sun-photometer. As the instrument measures direct solar radiation, it can only be used during day time and when the sun's disc is not obscured by clouds. This means that there are gaps in the Microtops measurement series, especially during the night time. In these gaps values of AOD were linearly interpolated.

AODs measured during the dust episode (Fig. 6) were noticeably higher than those observed on the other days. For example on April 13th (Fig. 6**a**) the optical depth at 500 nm wavelength reached 0.57 and on April 14th (Fig. 6**b**) – 0.67, in contrast to the values of 0.05–0.25 characteristic for days with no dust in the middle troposphere.
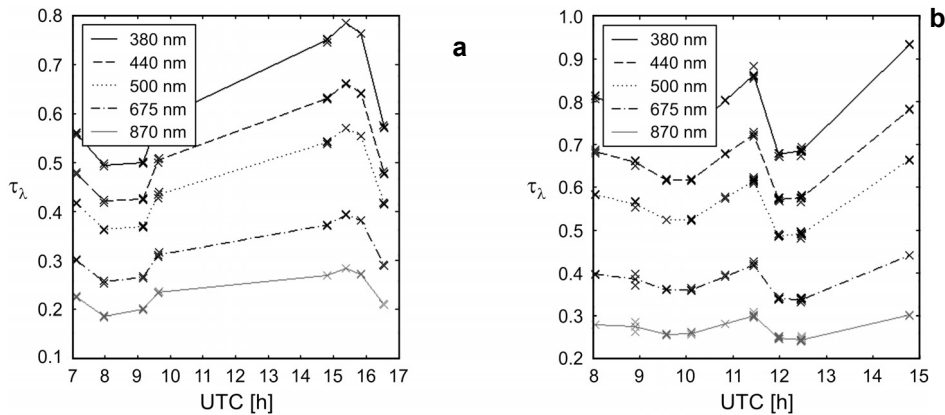

Fig. 6. Temporal evolution of AOD measured with Microtops on the 13 (**a**) and 14 (**b**) April 2005 in Warsaw.

Since Microtops channels do not overlap with the lidar ones, in order to estimate AODs in the lidar wavelengths, the Microtops measurements had to be transformed with the use of the Angstrom power law [32, 44]. As was already mentioned (Section 2), in the adopted procedure the atmosphere was divided into three layers: BL (presumably urban aerosols), DD with desert dust and CA above (Fig. 7). The first interface discriminating between BL and CA was assumed at the level of the local
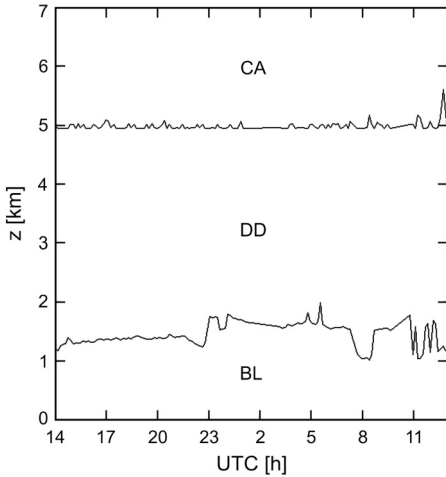
Fig. 7. Assumed division of atmosphere into three different layers – the boundary layer, the desert dust layer and the clear air layer.
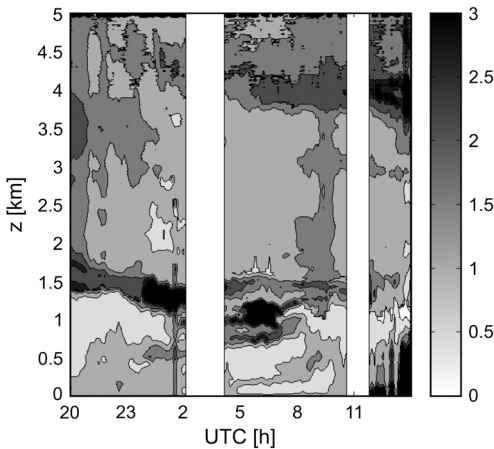

Fig. 8. Temporal evolution of light depolarization distribution measured by lidar at 532 nm wavelength, 13 – 14 April 2005, Warsaw. Relatively high depolarization values (grey layer between 1.2 and 4 km) correspond to mineral dust.

minimum of the lidar return signal (Fig. 1) between 1 and 1.5 km heights. The interface between DD and CA was set at the level of minimum aerosol depolarization, between 4.95 km and 5.6 km (Fig. 8). An independent cross-check of the adopted division has been performed with the use of ceilometer records [45], routine balloon sounding, and with the use of information from aerosol transport models NAAPS and HYSPLIT.

Estimates based on the preliminary application of Klett algorithm (considering atmosphere as a uniform layer) show that the optical thickness of DD (0.14 – 0.26 for 532 nm) was comparable to that of the BL (0.20 – 0.28 for 532 nm) – see Fig. 9. The estimated boundary layer AOD is consistent with the typical values observed in Warsaw apart from the dust episode. The linear increase in the total AOD during the night is the result of the interpolation.

From the lidar signals at 532 and 1064 nm distributions of extinction coefficients were derived, following the procedure described in Section 2.2. Figure 10 shows results for 532 nm wavelength, for times when the algorithm remained stable.
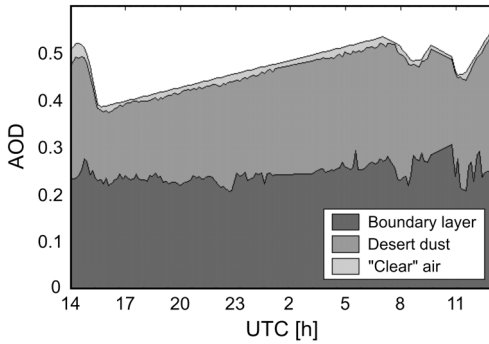
Fig. 9. Temporal evolution of AOD of atmospheric layers estimated on the basis of Microtops and lidar measurements on the 13–14 April 2005 in Warsaw (532 nm wavelength). Total AODs are linearly interpolated between measurement times.
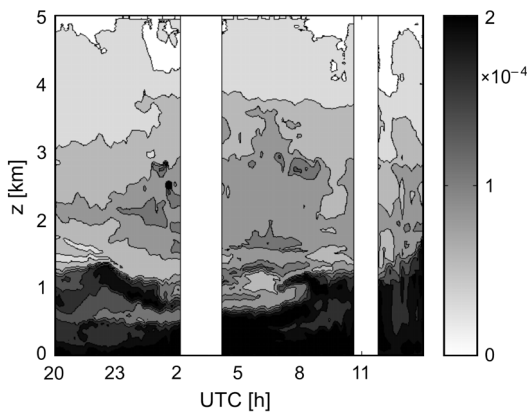

Fig. 10. Temporal evolution of aerosol extinction coefficient [1/m] vertical distribution estimated from lidar returns for the wavelength 532 nm on 13–14 April 2005.

Extinction coefficient in the desert dust layer is in the range of 0.5×10^{-4} m^{-1} to 1.5×10^{-4} m^{-1}. It is smaller than extinction coefficients in the BL, but as DD layer is relatively thick, its influence on radiative flux is important.

4.2. Modal size and characteristic aspect ratio of aerosol particles

Figure 11 shows fluctuations of vertical distribution of the local Angstrom exponent calculated from the extinction coefficients for 532 nm and 1064 µm wavelengths during the measurement period. Values in the BL (consult Fig. 11) are between 1.0 and 1.5, which corresponds to the particles of radii in the range of $0.22–0.27$ µm (see Fig. 4 and Tab. 1). Mean α increases up to 2.4 (Fig. 11**b**) in the layer between 1 and 1.7 km, in the transition region between boundary layer and desert dust layer. This value is uncertain, due to small values of extinction coefficient, indicating relatively small aerosol contents (*cf*. Figs. 10 and 11). Above this transition region (inside DD layer) Angstrom exponents are in the range of $1.2–1.8$ corresponding to the model size of particles $0.20–0.25$ µm. Between 3.8 and 4.2 km, the aerosol content is small again – estimated α are again high, but the reliability of retrieval is questionable. All
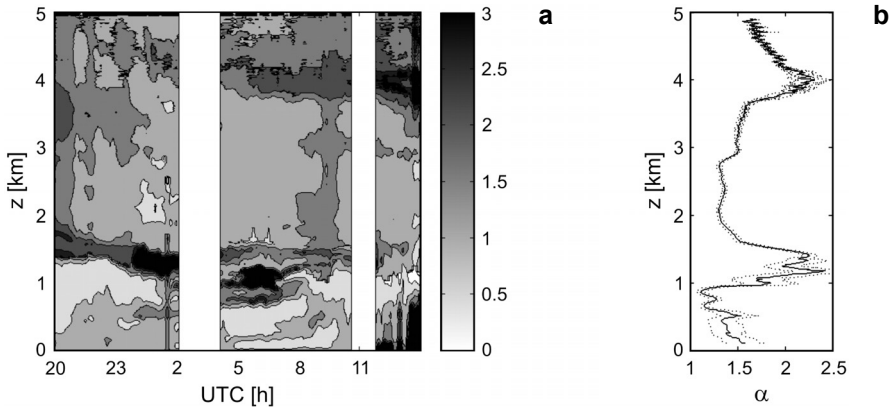
Fig. 11. Temporal evolution of Angstrom exponent vertical distribution calculated on the basis of aerosol extinction coefficients for 532 and 1064 nm wavelengths, on 13−14 April 2005 (**a**) and a mean Angstrom exponent α profile for the same measurement range (**b**). Dotted lines show the uncertainty range of the mean.

results are to some degree affected by the uncertainties introduced by lidar signal inversion procedure.

Figure 8 presents depolarization due to aerosol calculated for the 532 nm wavelength. We see that in DD layer depolarization is larger than 0.1 (mostly in the range of 0.12−0.15) and differs decidedly in BL where its value is close to zero. Figure 5 and Tab. 2 indicate that for such level of depolarization and mode radii 0.20−0.25 μm, the aspect ratios of spheroids representative for mineral dust are 0.6−0.8 for prolate spheroids or 1.3−2.0 for oblate spheroids. Maximum value of depolarization recorded − 0.18 corresponds to aspect ratios 0.6−0.8 or 1.4−2.2, respectively. Fortunately, in the range of particles sizes 0.20−0.25 the aspect ratio estimation is the least affected by the error resulting from unknown dust refractive index, resulting in only ~5% uncertainty.

4.3. Discussion

Observed high values of AOD − about 0.6 for 500 nm wavelength − are not surprising during the mineral dust episodes in Central Europe (*e.g.*, [9]) measured an increase in AOD from 0.25 to 0.63 for 532 nm during a Saharan aerosol outbreak 13−15.10.2001 over Leipzig in Germany.

In the aerosol layer identified as the mineral dust we noticed depolarization in the range of 0.1−0.18 for 532 nm wavelength. The upper limit of depolarization observed during SAWA was smaller than that reported by [9] and [11] (0.1−0.25). Estimated particle aspect ratios in the ranges of 0.6−0.8 or 1.3−2.2 are in agreement with the conclusion of [27] that aspect ratios of 1.5 and more are typical of the desert dust plumes.

What differs our results from [9, 18, 46] are relatively high values of Angstrom exponent. We cannot directly compare our results with above mentioned references

as different wavelengths are used for calculating α in each case. Our estimates in the DD layer show α in the range of $1.2-1.8$. These values are likely affected by the uncertainties introduced by the lidar signal inversion procedure, which may be significant in case of high AOD. However, after recheck of the photometric data, we ensured that neither Microtops nor AERONET measurements have revealed a single extraordinary drop of columnar Angstrom exponent, which could suggest the presence of larger particles. In addition, values of α (range $1.0-1.5$) in the boundary layer remained unchanged before, during and after the dust event. Combination of these information gives a support to the hypothesis that desert dust particles in this particular event over Warsaw were small.

Additional argument supporting this comes from the fact that the dust plume originated in Eastern and Central Sahara and in the Middle East. Reference [47] reports sizes of mineral dust collected in Israel (location in between the source regions) to be less than 1 µm in diameter for more than two thirds of particles. Lack of larger particles in the observed flow presumably results from intensive deposition observed in the Mediterranean before the plume reached Warsaw. According to [5], between the 10th and 11th of April (when according to HYSPLIT the plume passed over Crete) the increased values of total AOD, TOMS aerosol index and particle matter (PM10) concentrations were observed at Heraklion and Finokalia. They classify this event as *vertically extended transport* of mineral dust, with particles entering into the mixing layer and mixing with anthropogenic aerosol. On the other hand, the same mixing could add the anthropogenic aerosol into the plume and cause that maximum depolarization observed during SAWA was smaller than in reports of [9, 11].

5. Conclusions

A dust of episode $13-14$ April 2005 was analysed with synergistic measurements by the means of multi-wavelength lidar and Microtops sun-photometer. Synergy allowed to reduce the number of assumptions needed to estimate vertical profiles of extinction coefficients at 1064 and 532 nm wavelengths. Measurements and interpretation of numerical model allowed to distinguish three significantly different layers of aerosol: boundary layer with presumably local aerosol, the dust plume, and the clean free troposphere above. This was taken into account during the evaluation of the optical properties of aerosol from remote sensing data.

Estimated extinction profiles were combined with information on the depolarization of 532 nm wavelength. Observational data were compared to the numerical simulations of radiative transfer through a layer consisting of non-spherical particles, to estimate the properties of idealized particles that could represent mineral aerosol in a model. It was assumed that the mineral dust particles could be treated as an ensemble of spheroids of a given mode radii. This allowed performing calculations with the use of a T-matrix code and preparing look up tables to compare results of simulations with measurements. Comparison resulted in estimate of a mode radius and shape parameter (aspect ratio of a spheroid) of the observed mineral dust particles.

The estimates of Angstrom exponent in the mineral dust layer fall typically in the range of 1.2–1.8. Consequent estimates of mode radius are 0.20–0.25 μm, in agreement with the characteristic values for fine dust particles. No evidence of coarse particles on the dust plume was found. Observations of [5] support the hypothesis that they were deposited during the transport over the Mediterranean and Southern Europe.

Estimated values of AOD, of the depolarization ratio of 532 nm wavelength and estimates of shape (aspect ratio 0.6–0.8 or 1.3–2.2) are consistent with other reports available in the literature. Results of this study can contribute towards better parametrisation in modeling radiative processes for aerosol type *mineral transported* (*e.g.*, [41]).

References

[1] SOLOMON S., QIN D., MANNING M., CHEN Z., MARQUIS M., AVERYT K.B., TIGNOR M., MILLER H.L., [Eds.], *Climate Change 2007: The Physical Science Basis. Contribution of Working Group I to the Fourth Assessment Report of the Intergovernmental Panel on Climate Change*, Cambridge University Press, Cambridge 2007.

[2] SHINE K.P., FORSTER P.M.D.F., *The effect of human activity on radiative forcing of climate change: a review of recent developments*, Global and Planetary Change **20**(4), 1999, pp. 205–225.

[3] GOUDIE A.S., MIDDLETON N.J., *Saharan dust storms: nature and consequences*, Earth-Science Reviews **56**(1–4), 2001, pp. 179–204.

[4] ENGELSTAEDTER S., TEGEN I., WASHINGTON R., *North African dust emissions and transport*, Earth-Science Reviews **79**(1–2), 2006, pp. 73–100.

[5] KALIVITIS N., GERASOPOULOS E., VREKOUSSIS M., KOUVARAKIS G., KUBILAY N., HATZIANASTASSIOU N., VARDAVAS I., MIHALOPOULOS N., *Dust transport over the eastern Mediterranean derived from Total Ozone Mapping Spectrometer, Aerosol Robotic Network, and surface measurements*, Journal of Geophysical Research **112**, 2007, p. D03202.

[6] KARASIŃSKI G., KARDAŚ A.E., MARKOWICZ K., MALINOWSKI S.P., STACEWICZ T., STELMASZCZYK K., CHUDZYŃSKI S., SKUBISZAK W., POSYNIAK M., JAGODNICKA A.K., HOCHHERTZ C., WOESTE L., *LIDAR investigation of properties of atmospheric aerosol*, The European Physical Journal – Special Topics **144**(1), 2007, pp. 129–138.

[7] GOBBI G.P., BARNABA F., GIORGI R., SANTACASA A., *Altitude-resolved properties of a Saharan dust event over the Mediterranean*, Atmospheric Environment **34**(29–30), 2000, pp. 5119–5127.

[8] KUBILAY N., NICKOVIC S., MOULIN C., DULAC F., *An illustration of the transport and deposition of mineral dust onto the eastern Mediterranean*, Atmospheric Environment **34**(8), 2000, pp. 1293–1303.

[9] MÜLLER D., MATTIS I., WANDINGER U., ANSMANN A., ALTHAUSEN D., DUBOVIK O., ECKHARDT S., STOHL A., *Saharan dust over a central European EARLINET-AERONET site: Combined observations with Raman lidar and Sun photometer*, Journal of Geophysical Research **108**, 2003, p. D124345.

[10] BORBÉLY-KISS I., KISS A. Z., KOLTAY E., SZABÓ G., BOZÓ L., *Saharan dust episodes in Hungarian aerosol: Elemental signatures and transport trajectories*, Journal of Aerosol Science **35**(10), 2004, pp. 1205–1224.

[11] ANSMANN, A., BOSENBERG J., CHAIKOVSKY A., COMERON A., ECKHARDT S., EIXMANN R., FREUDENTHALER V., GINOUIX P., KOMGUEM L., LINNE H., MARQUEZ M.A.L., MATTHIAS V., MATTIS I., MITEV V., MULLER D., MUSIC S., NICKOVIC S., PELON J., SAUVAGE L., SOBOLEWSKY P., SRIVASTAVA M.K., STOHL A., TORRES O., VAUGHAN G., WANDINGER U., WIEGNER M., *Long-range transport of Saharan dust to northern Europe: The 11–16 October 2001 outbreak observed with EARLINET*, Journal of Geophysical Research **108**, 2003, p. D244783.

[12] FRANZEN L.G., HJELMROOS M., KALLBERG P., BRORSTROM-LUNDEN E., JUNTTO S., SAVOLAINEN A.L., *The 'yellow snow' episode of northern Fennoscandia, March 1991 – A case study of long-distance transport of soil, pollen and stable organic compounds*, Atmospheric Environment **28**(22), 1994, pp. 3587–3604.

[13] PAPAYANNIS A., AMIRIDIS V., MONA L., TSAKNAKIS G., BALIS D., BÖSENBERG J., CHAIKOVSKI A., DE TOMASI F., GRIGOROV I., MATTIS I., MITEV V., MÜLLER D., NICKOVIC S., PEREZ C., PIETRUCZUK A., PISANI G., RAVETTA F., RIZI V., SICARD M., TRICKL T., WIEGNER M., GERDING M., MAMOURI R.E., D'AMICO G., PAPPALARDO G., *Systematic lidar observations of Saharan dust over Europe in the frame of EARLINET (2000–2002)*, Journal of Geophysical Research **113**, 2008, p. D10204.

[14] GOBBI G.P., BARNABA F., BLUMTHALER M., LABOW G., HERMAN J.R., *Observed effects of particles nonsphericity on the retrieval of marine and desert dust aerosol optical depth by lidar*, Atmospheric Research **61**(1), 2002, pp. 1–14.

[15] BALIS D.S., AMIRIDIS V., NICKOVIC S., PAPAYANNIS A., ZEREFOS C., *Optical properties of Saharan dust layers as detected by a Raman lidar at Thessaloniki, Greece*, Geophysical Research Letters **31**, 2004, p. L13104.

[16] PAPAYANNIS A., BALIS D., AMIRIDIS V., CHOURDAKIS G., TSAKNAKIS G., ZEREFOS C., CASTANHO A.D.A., NICKOVIC S., KAZADZIS S., GRABOWSKI J., *Measurements of Saharan dust aerosols over the Eastern Mediterranean using elastic backscatter-Raman lidar, spectrophotometric and satellite observations in the frame of the EARLINET project*, Atmospheric Chemistry and Physics **5**(8), 2005, pp. 2065–2079.

[17] KISHCHA P., BARNABA F., GOBBI G.P., ALPERT P., SHTIVELMAN A., KRICHAK S.O., JOSEPH J.H., *Vertical distribution of Saharan dust over Rome (Italy): Comparison between 3-year model predictions and lidar soundings*, Journal of Geophysical Research **110**, 2005, p. D06208.

[18] LYAMANI H., OLMO F.J., ALADOS-ARBOLEDAS L., *Saharan dust outbreak over southeastern Spain as detected by sun photometer*, Atmospheric Environment **39**(38), 2005, pp. 7276–7284.

[19] FOTIADI A., HATZIANASTASSIOU N., DRAKAKIS E., MATSOUKAS C., PAVLAKIS K.G., HATZIDIMITRIOU D., GERASOPOULOS E., MIHALOPOULOS N., VARDAVAS I., *Aerosol physical and optical properties in the Eastern Mediterranean Basin, Crete, from Aerosol Robotic Network data*, Atmospheric Chemistry and Physics **6**(12), 2006, pp. 5399–5413.

[20] BALIS D., AMIRIDIS V., KAZADZIS S., PAPAYANNIS A., TSAKNAKIS G., TZORTZAKIS S., KALIVITIS N., VREKOUSSIS M., KANAKIDOU M., MIHALOPOULOS N., CHOURDAKIS G., NICKOVIC S., PEREZ C., BALDASANO J., DRAKAKIS M., *Optical characteristics of desert dust over the East Mediterranean during summer: a case study*, Annales Geophysicae **24**(3), 2006, pp. 807–821.

[21] GERASOPOULOS E., KOKKALIS P., AMIRIDIS V., LIAKAKOU E., PEREZ C., HAUSTEIN K., ELEFTHERATOS K., ANDREAE M.O., ANDREAE T.W., ZEREFOS C.S., *Dust specific extinction cross-sections over the Eastern Mediterranean using the BSC-DREAM model and sun photometer data: the case of urban environments*, Annales Geophysicae **27**(7), 2009, pp. 2903–2912.

[22] MARKOWICZ K.M., KARDAS A.E., *Retrieval of aerosol optical properties and estimation of aerosol forcing based on multi-spectral sun-photometer observations*, Proceedings of the 12th Conference on Cloud Physics, July 10–14, 2006, Madison, WI.

[23] WELTON E.J., VOSS K.J., GORDON H.R., MARING H., SMIRNOV A., HOLBEN B., SCHMIDT B., LIVINGSTON J.M., RUSSEL P.B., DURKEE P.A., FORMENTI P., ANDREAE M.O., *Ground-based lidar measurements of aerosols during ACE-2: instrument description, results and comparisons with other ground-based and airborne measurements*, Tellus B **52**(2), 2000, pp. 636–651.

[24] BÖCKMANN C., WANDINGER U., ANSMANN A., BÖSENBERG J., AMIRIDIS V., BOSELLI A., DELAVAL A., DE TOMASI F., FRIOUD M., GRIGOROV I.V., HÅGÅRD A., HORVAT M., IARLORI M., KOMGUEM L., KREIPL S., LARCHEVEQUE G., MATTHIAS V., PAPAYANNIS A., PAPPALARDO G., ROCADENBOSCH F., RODRIGUES J.A., SCHNEIDER J., SHCHERBAKOV V., WIEGNER M., *Aerosol lidar intercomparison in the framework of the EARLINET project. 2. Aerosol backscatter algorithms*, Applied Optics **43**(4), 2004, pp. 977–989.

[25] MISHCHENKO M.I., TRAVIS L.D., *Capabilities and limitations of a current FORTRAN implementation of the T-matrix method for randomly oriented rotationally symmetric scatterers*, Journal of Quantitative Spectroscopy and Radiative Transfer **60**(3), 1998, pp. 309–324.

[26] KAHNERT M., *Reproducing the optical properties of fine desert dust aerosols using ensembles of simple model particles*, Journal of Quantitative Spectroscopy and Radiative Transfer **85**(3–4), 2004, pp. 231–249.

[27] DUBOVIK O., SINYUK A., LAPYONOK T., HOLBEN B.N., MISHCHENKO M., YANG P., ECK T.F., VOLTEN H., MUNOZ O., VEIHELMANN B., VAN DER ZENDE W.J., LEON J.-F., SOROKIN M., SLUTSKER I., *Application of spheroid models to account for aerosol particle nonsphericity in remote sensing of desert dust*, Journal of Geophysical Research **111**, 2006, p. D11208.

[28] ROLPH G.D., *Real-time Environmental Applications and Display sYstem (READY)*, Website (http://www.arl.noaa.gov/ready/hysplit4.html), NOAA Air Resources Laboratory, Silver Spring, MD 2003.

[29] DRAXLER R.R., ROLPH G.D., *HYSPLIT (HYbrid Single-Particle Lagrangian Integrated Trajectory) Model access via NOAA ARL READY,* Website (http://www.arl.noaa.gov/ready/hysplit4.html), NOAA Air Resources Laboratory, Silver Spring, MD 2003.

[30] MORYS M., MIMS F.M., HAGERUP S., ANDERSON S.E., BAKER A., KIA J., WALKUP T., *Design, calibration, and performance of MICROTOPS II handheld ozone monitor and Sun photometer*, Journal of Geophysical Research **106**, 2001, pp. 14573–14582.

[31] HOLBEN B.N., ECK T.F., SLUTSKER I., TANRÉ D., BUIS J.P., SETZER A., VERMOTE E., REAGAN J.A., KAUFMAN Y.J., NAKAJIMA T., LAVENU F., JANKOWIAK I., SMIRNOV A., *AERONET – A federated instrument network and data archive for aerosol characterization*, Remote Sensing of Environment **66**(1), 1998, pp. 1–16.

[32] ANGSTROM A., *The parameters of atmospheric turbidity*, Tellus **16**, 1964, pp. 64–75.

[33] STELMASZCZYK K., DELL'AGLIO M., CHUDZYŃSKI S., STACEWICZ T., WÖSTE L., *Analytical function for lidar geometrical compression form-factor calculations*, Applied Optics **44**(7), 2005, pp. 1323–1331.

[34] LIU Z., SUGIMOTO N., MURAYAMA T., *Extinction-to-backscatter ratio of Asian dust observed by high-spectral-resolution lidar and Raman lidar*, Applied Optics **41**(15), 2002, pp. 2760–2767.

[35] BIELE J., BEYERLE G., BAUMGARTEN G., *Polarization lidar: Correction of instrumental effects*, Optics Express **7**(12), 2000, pp. 427–435.

[36] STEPHENS D.L., *Remote Sensing of the Lower Atmosphere*, University Press, New York, 1994.

[37] KLETT J.D., *Stable analytical inversion solution for processing lidar returns*, Applied Optics **20**(2), 1981, pp. 211–220.

[38] FERNALD F.G., *Analysis of atmospheric lidar observations: some comments*, Applied Optics **23**(5), 1984, pp. 652–653.

[39] WATERMAN P.C., *Symmetry, unitarity, and geometry in electromagnetic scattering*, Physical Review D **3**(4), 1971, pp. 825–839.

[40] MISHCHENKO M.I., TRAVIS L.D., KAHN R., WEST R.A., *Modeling phase functions for dustlike tropospheric aerosols using a shape mixture of randomly oriented polydisperse spheroids*, Journal of Geophysical Research **102**, 1997, pp. 16831–16847.

[41] HESS M., KOEPKE P., SCHULT I., *Optical properties of aerosols and clouds: The software package OPAC*, Bulletin of the American Meteorological Society **79**(5), 1998, pp. 831–844.

[42] KALASHNIKOVA O.V., SOKOLIK I.N., *Modeling the radiative properties of nonspherical soil-derived mineral aerosols*, Journal of Quantitative Spectroscopy and Radiative Transfer **87**(2), 2004, pp. 137–166.

[43] NOUSIAINEN T., KAHNERT M., VEIHELMANN B., *Light scattering modeling of small feldspar aerosol particles using polyhedral prisms and spheroids*, Journal of Quantitative Spectroscopy and Radiative Transfer **101**(3), 2006, pp. 471–487.

[44] SCHUSTER G.L., DUBOVIK O., HOLBEN B.N., *Angstrom exponent and bimodal aerosol size distributions*, Journal of Geophysical Research **111**, 2006, p. D07207.

[45] MARKOWICZ K.M, FLATAU P.J., KARDAS A.E., REMISZEWSKA J., STELMASZCZYK K., WOESTE L., *Ceilometer retrieval of the boundary layer vertical aerosol extinction structure*, Journal of Atmospheric and Oceanic Technology **25**(6), 2008, pp. 928–944.

[46] TAFURO A.M., BARNABA F., DE TOMASI F., PERRONE M.R., GOBBI G.P., *Saharan dust particle properties over the central Mediterranean*, Atmospheric Research **81**(1), 2006, pp. 67–93.

[47] KOREN I., GANOR E., JOSEPH J.H., *On the relation between size and shape of desert dust aerosol*, Journal of Geophysical Research **106**, 2001, pp. 18047–18054.